

3D flow visualization and tomographic particle image velocimetry for vortex breakdown over a non-slender delta wing

ChengYue Wang¹ · Qi Gao¹ · RunJie Wei³ · Tian Li^{1,2} · JinJun Wang¹

Received: 1 November 2015 / Revised: 4 May 2016 / Accepted: 9 May 2016 / Published online: 24 May 2016
© Springer-Verlag Berlin Heidelberg 2016

Abstract Volumetric measurement for the leading-edge vortex (LEV) breakdown of a delta wing has been conducted by three-dimensional (3D) flow visualization and tomographic particle image velocimetry (TPIV). The 3D flow visualization is employed to show the vortex structures, which was recorded by four cameras with high resolution. 3D dye streaklines of the visualization are reconstructed using a similar way of particle reconstruction in TPIV. Tomographic PIV is carried out at the same time using same cameras with the dye visualization. Q criterion is employed to identify the LEV. Results of tomographic PIV agree well with the reconstructed 3D dye streaklines, which proves the validity of the measurements. The time-averaged flow field based on TPIV is shown and described by sections of velocity and streamwise vorticity. Combining the two measurement methods sheds light on the complex structures of both bubble type and spiral type of breakdown. The breakdown position is recognized by investigating both the streaklines and TPIV velocity fields. Proper orthogonal decomposition is applied to extract a pair of conjugated helical instability modes from TPIV data. Therefore, the dominant frequency of the instability modes is obtained from the corresponding POD coefficients of the modes based on wavelet transform analysis.

1 Introduction

The flow structures behind a delta wing have stimulated a great deal of investigating interest since its important roles in controlling the aerodynamic performances of the wing. At low incidence, a pair of counter-rotating leading-edge vortices (LEVs) dominates the leeward flow. As the increase in incidence, the LEVs would suddenly lose instability and breakdown when they travel downstream over the wing, bringing significant change in both flow structures and unsteady aerodynamic characteristics (Gursul 2005).

Lambourne and Bryer (1962) discovered two typical types of breakdown over a delta wing: bubble type and spiral type. Subsequent experimental investigations have been focused on the characteristics of the breakdown phenomenon and its onset position above the wing. The experiments showed that while the two types of vortex breakdown switched to each other from time to time, the spiral type happened more often than the bubble type (Gursul 2005). Coherent oscillation was found downstream the breakdown location by the pressure measurement on the wing plane (Gursul 1994). The corresponding dimensionless frequency (fx/U_∞) by streamwise position x and free-stream velocity U_∞ is nearly constant for a given geometry of the delta wing, which implies an increasing wavelength of the disturbance in the streamwise direction (Gursul 1994). In a column coordinate (x, ψ, r) , the disturbance downstream to the breakdown position could be theoretically predicted by $\text{Exp}[i(kx + n\phi - \omega t)]$, where ω is the frequency, k is the wave number in the axial direction, and n is the wave number in the angular direction (Lessen et al. 1974). The breakdown position is not fixed and exhibits oscillation in the streamwise direction. Spectral analysis on such oscillation reveals a peak on a very low frequency, which completely

✉ Qi Gao
qigao@buaa.edu.cn

¹ Key Laboratory of Fluid Mechanics, Ministry of Education, Beijing University of Aeronautics and Astronautics, Beijing 100191, China

² Shenyang Aircraft Design and Research Institute, Shenyang 110035, China

³ MicroVec., Inc, Beijing 100083, China

differs from the one caused from the helical mode instability or the Kelvin–Helmholtz instability and indicates that the oscillation is a new instability (Gursul and Yang 1995). Different theoretical models of the vortex breakdown including hydrodynamic instability, wave propagation and flow stagnation have been summarized in several review articles (e.g., Hall 1972; Escudier 1988; Lucca-Negro and O’doherly 2001). It has been well concluded that the swirl level and external pressure gradient outside the vortex core are the two most important facts affecting the occurrence and streamwise position of the breakdown. Enhancements of both facts would promote the breakdown earlier (Gursul 2005).

Earlier investigations on the LEV breakdown have been mainly focused on the slender delta wings. However, recent developments in micro-air vehicles (MAVs) and unmanned combat air vehicle (UCAV) have inspired the investigations on non-slender delta wings. The non-slender delta wings distinguished by a sweep angle less than 55° (Gursul et al. 2005) exhibit quite different flow structures to the slender ones. One typical unique characteristic of the non-slender delta wing is the dual-vortex structure at specific incidences and Reynolds numbers, which was experimentally discovered and investigated by Taylor et al. (2003), Yaniktepe and Rockwell (2004) and Wang and Zhang (2008). The vortices were closer to the upper surface of the delta wing, leading to strong interaction with the boundary layer and pronounced dependence of flow structures on Reynolds numbers (Gursul et al. 2002; Taylor et al. 2003). The work of Ol et al. (2003) exhibited a special wake-like velocity profile near the LEV core upstream the breakdown position at a low Reynolds number, while, at a higher Reynolds number, a jet-like velocity profile was observed which was similar to vortices over slender delta wing (Gursul et al. 2005). It was also reported that vortex breakdown location shows more significant fluctuations in the streamwise direction (Taylor et al. 2003; Ol et al. 2003). It seems that the unsteady characteristics of the breakdown phenomenon behind a non-slender delta wing are more complex than the slender one.

Most of the earlier investigations on the vortex breakdown are based on visualization. The dye or smoke released from the apex could visualize the LEVs with clear streaklines. The streaklines exhibit the detailed shape of LEVs and indicate the breakdown positions by sudden expansion or diffusion of the streaklines. Therefore, the visualization method is very straightforward and has been widely used to recognize the breakdown position and type (Lambourne and Bryer 1962; Gursul and Yang 1995). However, the method fails to quantitatively provide any dynamic information of the flow. Any one-point or 2D measurement such as particle image velocimetry (PIV) could provide quantitative experimental data, but hardly capture a complete

LEV since the LEV’s spatial and temporal complexities. By employing defocusing digital PIV (Pereira and Gharib 2002), Calderon et al. (2012) achieved three-dimensional and three-component (3D3C) velocity fields over a non-slender and periodically plunging delta wing, discovering a very rare type of breakdown, the double helix. On the other hand, tomographic PIV (TPIV) method (Elsinga et al. 2006; Scarano 2013) is also a sophisticated technique on measuring volumetric flow fields with better spatial resolution. However, the computation of TPIV is quite time-consuming. Therefore, it would be instructive to get some qualitative information from flow visualization about the breakdown phenomenon before applying the time-consuming TPIV processing. The dye visualization method could easily capture the right snapshot of the breakdown with a clear breakdown position and type, which would also be a good supplement for the TPIV measurement.

In the current work, the breakdown phenomenon over a non-slender delta wing is simultaneously investigated by the dye visualization and TPIV measurement. The images of dye streakline and PIV tracer particles are recorded by four shared high-resolution cameras at the same time. Subsequently, the images of dye streakline are separated from the particles, and three-dimensional (3D) dye streaklines are reconstructed, which provide a comparative reference and also an important supplement for the results of TPIV. The article is arranged in the following fashion. Section 2 introduces detailed information about the dye visualization and TPIV measurement. Some processing techniques including the ways of extracting the dye streakline images, reconstructing 3D dye streaklines and calculating the TPIV velocities are also provided in the section. Section 3 discusses the results of the measurement followed by a conclusion in Sect. 4.

2 Experimental setup and methodology

2.1 Experimental setup

The experiment was conducted in a circular open water tunnel in Beijing University of Aeronautics and Astronautics, China. The size of the test section is $3000\text{ mm} \times 600\text{ mm} \times 700\text{ mm}$ in streamwise, spanwise and vertical directions, respectively. The free-stream velocity U_∞ could be adjusted up to 300 mm/s with a motor controller. A schematic of the experimental setup is shown in Fig. 1a. The model of delta wing has a sweep angle of 52° , which falls in the non-slender delta wing category. The model was manufactured using duralumin, with black spray paint to reduce surface reflection under laser illumination. The length of root chord (c) is 200 mm and the thickness of the model is about 3 mm , resulting in a thickness-to-chord

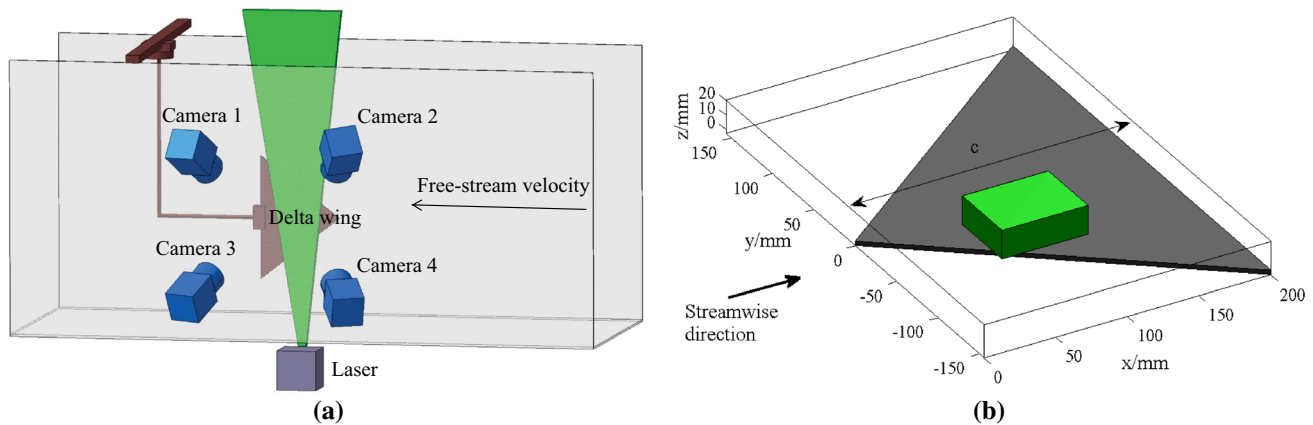


Fig. 1 Experimental setup (a) and the coordinate system (b)

ratio of 1.5 %. Since the delta wing is very thin, the leading shape would not cause much difference to the vortex structure. Therefore, a simple plane edge with no beveling on both sides was employed in the current experiment. The model was firmly mounted with a stiff sting from its windward face. The disturbance of the support to the flow was negligible and no notable model vibrations were observed in the experiment. The same model and corresponding support setup were employed as a baseline model by Chen and Wang (2014).

In the experiment, the origin of the coordinate was set at the apex of the delta wing. Three axes (x , y , z) of the coordinate were along the chord-wise, spanwise and plane-normal directions, respectively. The measurement volume was in the coordinate range of $[66, 126] \times [-63, -15] \times [0, 20]$ (mm), which would contain the breakdown location as the green box shown in Fig. 1b. All the following processing works including reconstructing dye streaklines and calculating for TPIV were carried out in the measurement volume.

The delta wing was mounted at an incidence of 20° for generating the breakdown in the measurement volume. A tiny pipe with a diameter of about 2mm was stuck on the windward face of the wing and extend to the apex with a needle (about 1mm) to release the dyeing liquid, which is a standard manner of dye visualization (Ol et al. 2003). To ensure that the dyeing fluid did not affect the formation of the LEV, the exit velocity of dye was carefully adjusted. A little amount of rhodamine was added to the dye liquid to make the dye visible under the laser light. Silver-coating hollow particles with mean diameter of $50 \mu\text{m}$ were seeded as tracers in the water channel. A dual-head ND:YAG laser with 500 mJ/pulse was equipped to generate a thick light sheet with thickness of 20 mm, paralleled to and 1 mm away from the platform of the delta wing. Four high-resolution (2058×2456 pixels², 12 bit) and double-exposure

cameras (IMPERX B2520) were squarely arrange to image the measurement volume from different viewing angles of $\sim 25^\circ$ as shown in Fig. 1a. 45 mm Nikon lenses with f number of 11 were used in the experiment. The repetition frequency for the measurement system was 5 Hz. A timing device was employed to make the measurement devices synchronized. The free-stream velocity was adjusted to 60 mm/s, and the corresponding Reynolds number based on the root chord was about 12000. The turbulent intensity of the free-stream flow was less than 2 %. The images of dye streaklines and tracing particles were recorded simultaneously by the cameras. In order to separate the two types of images easily, the intensity of dye streakline should be weaker than the particles, but stronger than the background noise. Therefore, the mount of rhodamine needed to be adjusted very carefully to optimize the imaging quality.

2.2 Separating dye streakline from a particle image

A typical image from the recording cameras is displayed in Fig. 2a. There are two obvious differences between the images of the dye streaklines and the tracer particles. First, intensities of the dye streaklines are much lower than the particle intensities, which is due to the little amount of rhodamine mixed in the dye. Second, the dye streaklines appear as clusters with large connected zones, while the particles are individually distributed. In fact, the particle images occupy typically 3×3 or 5×5 pixels in the measurement.

According to these differences, a corresponding streakline-separating algorithm was designed, as shown in Fig. 2a and detailed as the following corresponding steps:

1. Select object zone. A small object zone containing the dye streaklines in the raw image is specially selected as shown in Fig. 2a. The step would accelerate the pro-

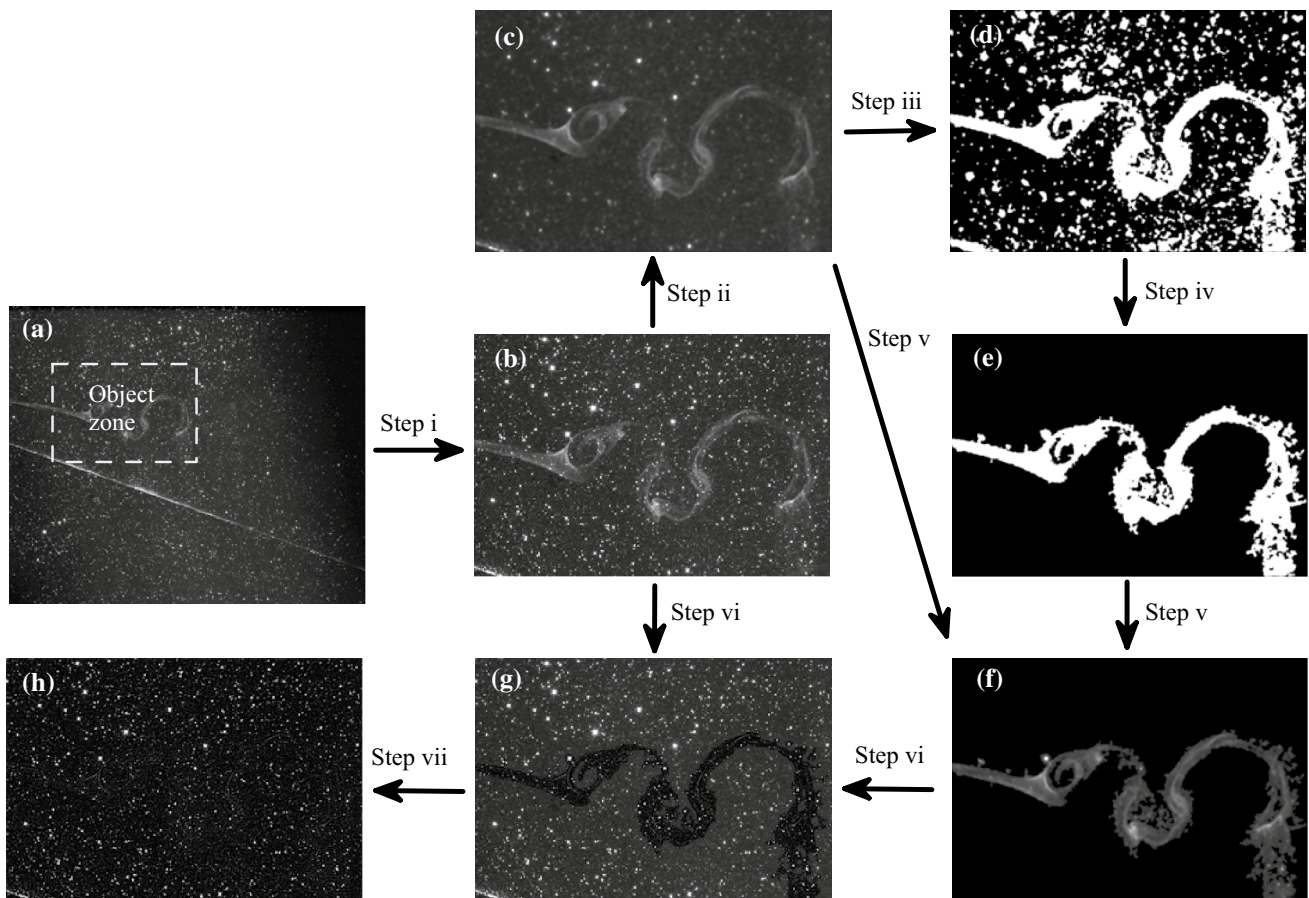


Fig. 2 A sketch for the separating procedures. The *images* produced in every processing step are displayed separately. *Black arrows* indicate the processing flow

1. Process the image to identify the object zone and avoid the confusing particle images and background noise outside the object zone.
2. Apply the median filter. A 9×9 (larger than the size of most particles) median filtering is employed to reduce most particles, remaining the dye streaks and few large clustered particles. In the current test, the recorded dye streakline normally had more than 20 pixels in width, which means the filtering procedure would hardly reduce its size or blur the intensity distribution on it. The step would make the dye streakline easier to be distinguished from the images, as shown in Fig. 2c.
3. Binarize the intensities. Image in Fig. 2c is further binarized by comparing pixel intensities with a threshold value. The threshold of the intensity is set as the median value of intensities multiplied by 1.2 in the present experiment, which is a robust estimation for the upper limit of the background noise. The binarizing process cleans the background noise and produces an image with several connected binary domains as shown in Fig. 2d.

4. Identify the connected zones. To extract the streakline from Fig. 2d, a connected domain detection is performed. Only the largest few domains are labeled as the dye streakline. The criterion for selected domains depends on the estimation for the sizes of the broken pieces of dye streakline. In the current work, the connected zones with areas larger than 10 % of the largest connected region in the image were considered as the parts of dye streaklines. In the example shown in Fig. 2, only one connected zone is selected to get an identified image as shown in Fig. 2e.
5. Isolate the streakline. With the binary image of Fig. 2e, the streakline in Fig. 2c can be easily extracted by simply multiplying the intensity matrix of Fig. 2c with the binary matrix of Fig. 2e. The separated images of dye streakline as shown in Fig. 2f will be used for 3D dye reconstruction in Sect. 2.3.
6. Remove the dye streakline from the raw image. The particle image (Fig. 2g) is obtained by subtracting the streakline (Fig. 2f) from the raw image (Fig. 2b).

7. Remove the background from the separated particle image. Figure 2g exhibits a shadow of streakline, which is expectable since the subtracted streakline contains some background intensities. To reduce the influence of the shadow and also as a common procedure for TPIV preprocess, the median intensity from a 11×11 neighboring zone was subtracted from Fig. 2g to remove the background noise (Scarano 2013). The result as shown in Fig. 2h is a well-processed particle image for TPIV.

The above separating algorithm contains several experienced parameters, which would depend on specific experimental configurations. The trick for a successful separation of dyes and particles is an appropriate concentration of the dye. A thick and bright streakline would be easier for being distinguished from the background noise, but also lead to difficulty in cleaning up its remnants from the particle image. A balance is needed to achieve both good streakline images and particle images. In the current work, the high quality of particle images is of the highest priority, considering that the importance of TPIV results in the quantitative investigation. Therefore, a dye mixed with low-concentrated rhodamine is employed in the current work as shown in Fig. 2.

2.3 Reconstruction for dye streakline

After separating the dye streaklines from the raw images, the multiplicative algebraic reconstruction technique (MART) algorithm (Elsinga et al. 2006) was used to reconstruct 3D streaklines. For TPIV reconstruction, the voxel-to-pixel rate is normally set to 1. To accelerate the streakline reconstruction, the rate was set to 4, resulting in a coarser spatial grid and less computational cost. The corresponding voxel size was 0.22 mm, which was fine enough to qualitatively visualize the 3D LEV, as presented in Sect. 3.2.

2.4 Calculation for tomographic PIV

The particle images removed background as shown by Fig. 2h went through a traditional TPIV process. Self-calibration technique was employed to improve the accuracy of the mapping function (Wieneke 2008), which made the regular disparity error of the original mapping functions of ~ 0.5 pixels reduced to be less than 0.1 pixels. A traditional TPIV processing was employed by an in-house MATLAB code. MART algorithm with a voxel-to-pixel rate of 1 was employed to reconstruct the 3D particle intensity field, resulting in volume size of $1091 \times 873 \times 364$ voxels with magnification of 0.055 mm per voxel. Multi-pass correlation analysis with deforming investigating

window (Scarano 2002) was applied to calculate the 3D velocity fields. The final investigating window size was $48 \times 48 \times 48$, and the overlap rate was 50 %, leading to a spatial resolution of 2.64 mm, which was 1.32 % of the root chord length. The particle seeding density was about 0.035 particles/pixel, which was calculated by counting intensity peaks in the images. Statistically, about 10 particles were found in a correlation volume with size of 48^3 voxel cube, which was suitable for a robust cross-correlation analysis (Scarano 2013). The resulting velocities distributed on a $44 \times 35 \times 15$ spatial grid corresponding a physical domain in the coordinate (x, y, z) range of $[67.3, 124.1] \times [-61.7, -16.8] \times [1.3, 19.8]$ (mm). Totally 100 time-sequential velocity fields were deduced. The velocity fields were processed by a divergence-free smoothing algorithm (Wang et al. 2016). The uncertainty for velocity was estimated as less than 0.2 pixel (similar to Elsinga et al. 2006), which corresponded to 3.5 % of the free-stream velocity. The uncertainty for velocity gradient was estimated as about $5U_\infty/c$ under the 2-order central difference scheme.

3 Results and discussion

At a low incidence, the flow passing the delta wing is dominated by a pair of primary vortices (LEVs). At an incidence of about 10° , another pair of primary vortex structures occurs outside the original ones, forming a special dual primary vortex structure (Chen and Wang 2014). At a larger incidence of 20° , the dual-vortex structure turns back into the single-pair vortex status, which is also observed in the following results.

3.1 Time-averaged flow

The time-averaged velocity field and streamwise vorticity ω_x field are presented in Fig. 3. Three spanwise and plane-normal sections at $x/c = 37.6\%$ (I), 47.5% (II) and 57.4% (III) are selected to show the three-dimensional fields. Another two edge sections at $z = 1.3$ mm and $y = -16.8$ mm are also plotted for better visualizing the flow field. In Fig. 3a, the field is shown with the in-plane velocity vectors and the contours of the magnitude of the streamwise velocity. The velocities are normalized by the free-stream velocity U_∞ . In Fig. 3b, the streamwise vorticity normalized by U_∞ and root chord length c is displayed by contours. At section I, the separated shear layer, which results from the leading edge, rolls into a strongly rotated vortex, namely LEV. A secondary vortex with weaker vorticity and opposite rotating direction is formed near the LEV due to the inducing effect. The velocity distribution at the LEV core presents a jet-like profile (Taylor and Gursul 2004). As

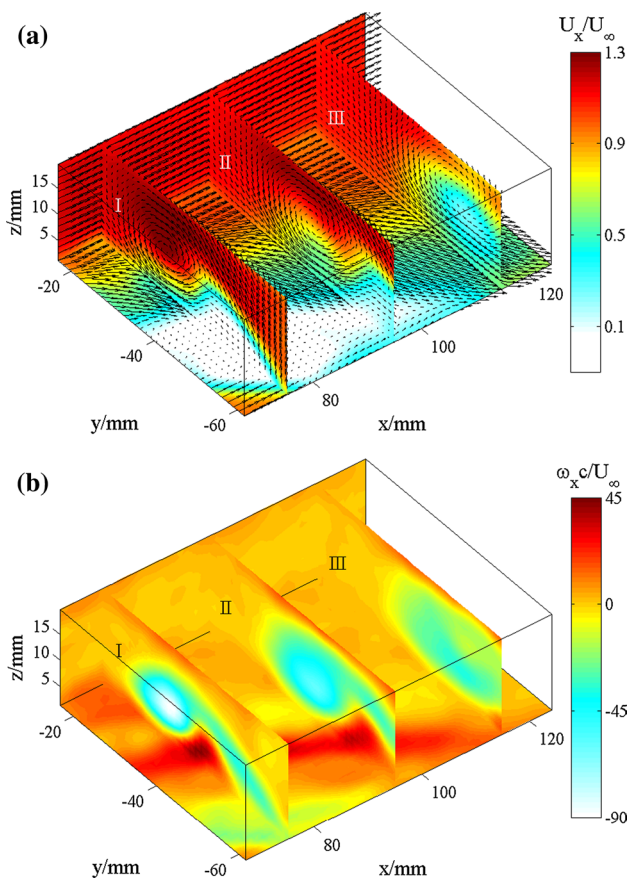


Fig. 3 Time-averaged velocity field (a) and streamwise vorticity field (b). Three spanwise and plane-normal sections of $x/c = 37.6\%$ (I), 47.5% (II) and 57.4% (III), and two edge sections at $z = 1.3$ mm and $y = -16.8$ mm are visualized

LEV travels downstream to section II, both velocities and vorticities near the LEV core are reduced. The size of the vortex core increases and jet-like profile becomes broad. At section III, the LEV core has been significantly diffused to a very weak vortex, and a wake-like profile is observed. The spatial evolution of the vortex structures from section I to section III reveals the occurrence of vortex breakdown, which will be further discussed in the following subsections. These observations exhibit some similarities to slender wings at relatively higher incidences. However, the switch of the velocity profiles happening over a non-slender delta wing is not as abrupt as the corresponding switch on a slender delta wing (Gursul et al. 2005).

The LEV structure of a delta wing with a sweep angle of 50° at an incidence of 15° was experimentally studied by Taylor and Gursul (2004) and numerically investigated by Gordnier and Visbal (2005) at a similar Reynolds number of about 26,000. Both studies found a switching phenomenon from a jet-like flow at the upstream of the breakdown to a wake-like flow at the downstream of the breakdown. Differently, Ol et al. (2003) observed a wake-like profile

even at the upstream of the breakdown for a delta wing with same sweep angle and incidence, but at a lower Reynolds number of 8500. In the current experiment, at larger incidence of 20° and a larger Reynolds number of 12,000, the profile-switch phenomenon was also observed. It seems that the incidence and Reynolds number have profound influence on the LEV structures of a non-slender delta wing.

3.2 Visualization of vortex breakdown

The visualization of LEV is an important step for further analyzing on the breakdown phenomenon. Herein, we have two ways to extract LEV: visualizing streakline with dye and applying vortex identification method based on the TPIV data. The dye visualization shows streakline of LEV with iso-surface of the dye concentration. The threshold of the iso-surface is set to be one-fourth of the average dye concentration of the streakline. The TPIV data are employed to calculate the Q criterion (Hunt et al. 1988) by

$$Q = (|\Omega|^2 - |\mathbf{S}|^2)/2, \quad (1)$$

where Ω and \mathbf{S} are the angular velocity tensor and the rate of strain tensor, respectively. $|| \cdot ||$ represents the Euclidean norm. The criterion has been widely employed for vortex identification (e.g., Calderon et al. 2012). The iso-surface of $Qc^2/U_\infty^2 = 333.3$ is applied to visualize the LEV. A Gaussian smoothing with size of $3 \times 3 \times 3$ and $\sigma = 0.65$ is employed as a post-processing to reduce the background noise on Q -identified field.

Results about LEV identified by both dye streakline and Q criterion are presented in Fig. 4. Two instantaneous fields corresponding to two types of breakdown are shown. For the spiral-type breakdown (Fig. 4a, b), the dye visualization shows a clear helical swirl motion. The pitch (wavelength) of the helix increases in the streamwise direction, which is consistent with the results for slender delta wings (Towfighi and Rockwell 1993). It suggests that the LEV still retains a strong swirl after the breakdown, which could be clearly identified by Q criterion as well, as shown by green surfaces in Fig. 4b. Although the dye streakline and the Q -identified LEV present different kinds of information from the flow, they indicate a consistent characteristic of a spiral LEV in this case. The low-speed zone (stagnation) is also shown in the result of TPIV, which is represented by two blue iso-surfaces of LEV axial velocity $U_{\text{axial}}/U_\infty = 0.2$ and $U_{\text{axial}}/U_\infty = 0$ (the way of determining the LEV axis will be discussed in Sect. 3.3). It reveals that a recirculating flow occurs downstream the vortex breakdown, which is a notable phenomenon of the helical swirl at the downstream of breakdown Gursul et al. (2005). As shown in the figure, the sense of the helix is opposite to the rotating direction of the LEV, which was also reported by Srinivas et al. (1994).

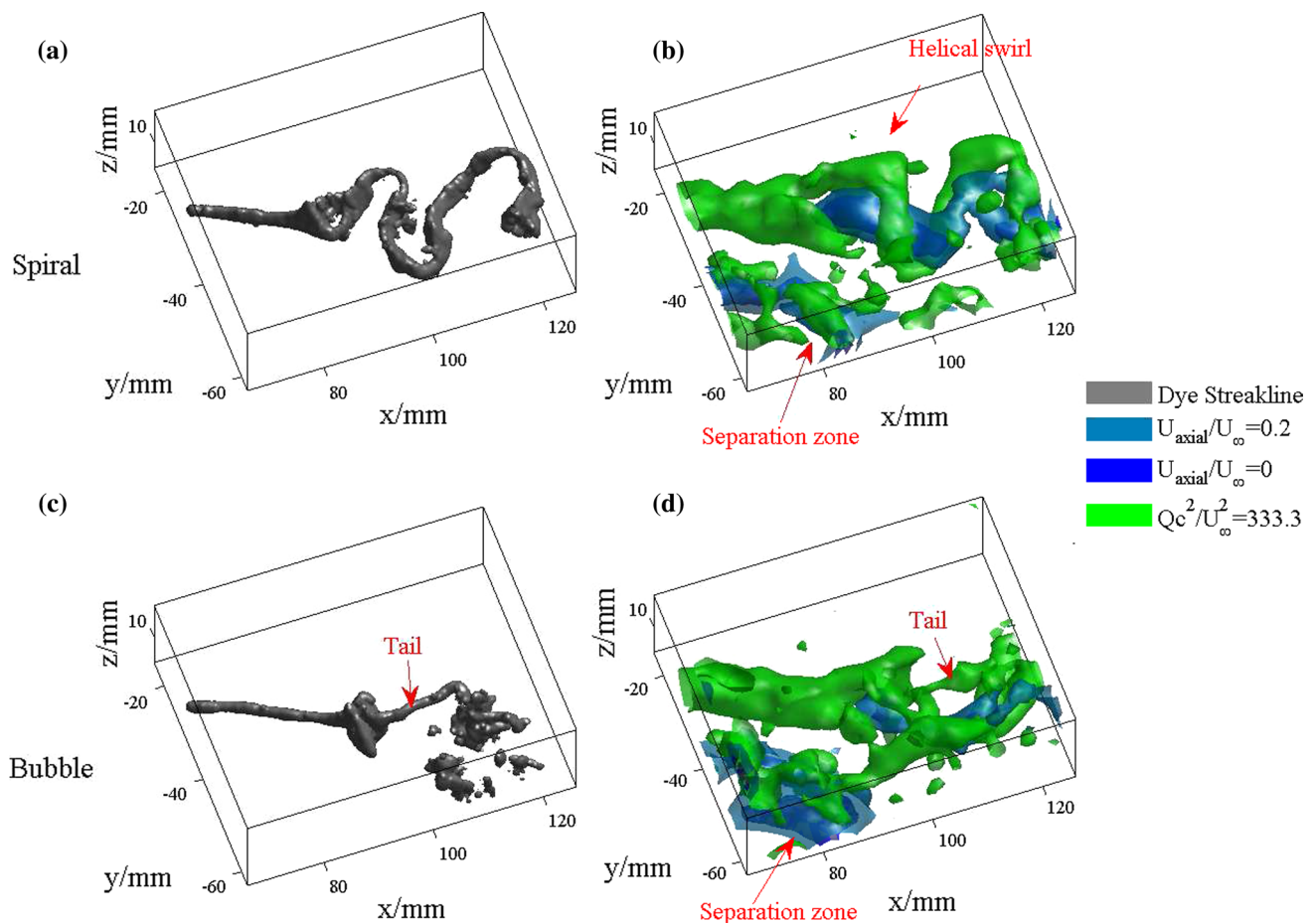


Fig. 4 Visualization of LEV for spiral-type breakdown (a, b) and bubble-type breakdown (c, d). a, c Show the iso-surfaces of dye concentration (1/4 of the average dye concentration). b, d Visualize the

iso-surfaces of $Qc^2/U_{\infty}^2 = 333.3$ (green), $U_{axial}/U_{\infty} = 0.2$ (light blue) and $U_{axial}/U_{\infty} = 0$ (deep blue)

Such helical swirl would produce a upstream velocity due to the Biot–Savart induction, resulting in a recirculating flow as pointed out by Jumper et al. (1993). The separation zone is also observed nearby the LEV close to the leading edge, with small vortices produced by Kelvin–Helmholtz (KH) instability (Gursul 2005).

The bubble type is normally characterized by a sudden expansion of LEV (Escudier 1988) as shown in Fig. 4c and d. The dye streakline exhibits a tailing streakline after the expansion, which persists for certain distance before it completely breaks. The iso-surface of Q shows a similar expansion to the dye streakline. A stagnation zone occurs downstream the breakdown position, but with comparatively small recirculating zone ($U_{axial}/U_{\infty} \leq 0$). A thin vortex tube happens at the place where the tailing dye streakline occurs. Other vortex structures also exist in the downstream region of breakdown, which indicates the highly instability of bubble-type breakdown.

It has been clearly noticed that the 3D dye streaklines (Fig. 4a, c) provide detailed presentation for LEV structure,

which is an important reference and supplement for TPIV measurement. To further study the motion of helix, we extracted the skeletons from the dye streaklines (Lee et al. 1994; Kerschitzki et al. 2013) and fitted them by smoothing splines, resulting in helical lines as shown in Fig. 5. Three helical lines (α , β , γ) were extracted from three time-sequential dye fields when spiral-type breakdown appears. The time interval between two neighbors is 0.2 s, which corresponds to a 5 Hz repetition frequency. The helical lines are displayed in Fig. 5 by two views: oblique view (a) and axial view (b), which are attributed to the application of the new qualitative visualization technique. The viewing angle of the oblique view is consistent with the view of Fig. 4, while the axial view shows the lines from the LEV axial direction (downstream to upstream). The figure clearly displays a rapid increase in helix pitch. These helical lines are similar to each other, with almost a constant phase shift, rotating in the same direction with the LEV swirl. The rotation motion of helix structure is a result of the helical mode instability, which would induce periodic

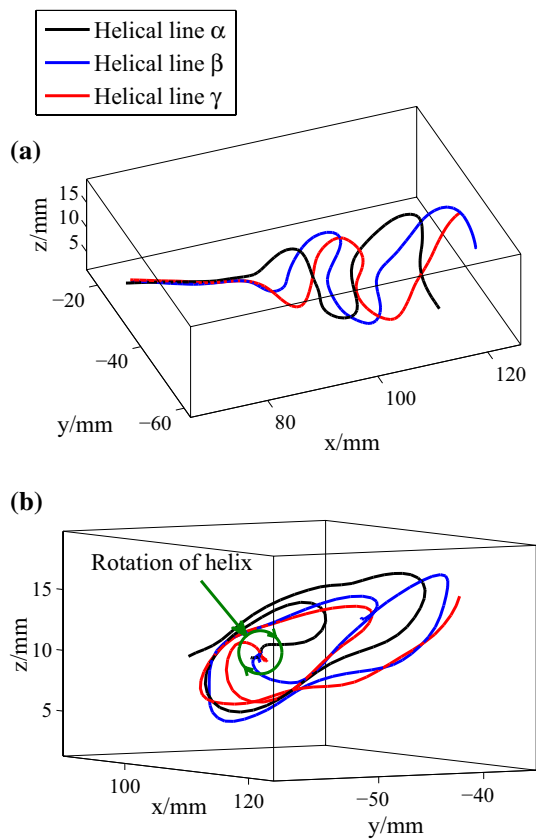


Fig. 5 Helical lines extracted from dye streaklines and displayed by the oblique view (a) and axial view (b). Helical lines (α , β , γ) correspond to three neighboring sampling times in the experiment

fluctuation downstream the breakdown location (Gursul et al. 2005). By observing the phase angles of the three helical lines on the axial view plot, the angular frequency of helix is roughly estimated between 1 and 2 Hz, which will be quantitatively studied using wavelet analysis in Sect. 3.4. It is worth noting that the projected trajectories in Fig. 5b do not show a standard circular pattern as predicted by many theoretical models (Lessen et al. 1974). In fact, the pattern is more like an inclined ellipse. The reason could probably be explained as the bounding effect of the boundary layer here, because the LEV for a non-slender delta wing is very close to the the boundary as reported by Gursul et al. (2002).

3.3 Oscillation of breakdown position

In this section, the vortex breakdown positions are investigated in two ways: the dye streaklines and TPIV velocity fields. Sectional intensity integrations (SIIs), defined as the integration of dye intensity in the plane normal to the streamwise direction, are calculated at different streamwise locations. SIIs are strongly associated with dye streaklines,

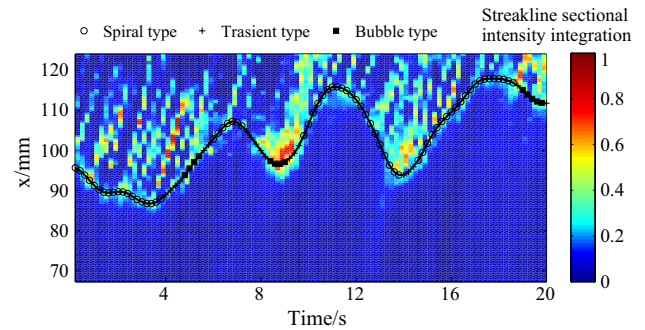


Fig. 6 The vortex breakdown positions and types based on the dye streaklines. The *contour* denotes SII, normalized by the largest value. The breakdown positions for different instantaneous times based on the SII distribution are displayed by a *black line*. Breakdown types are marked on the line by *hollow circles* (spiral), *cross symbols* (transient) and *solid squares* (bubble)

which could be used as a reference to the breakdown positions. The breakdown types are also recognized by the characteristics of the instantaneous streaklines. Meanwhile, regions of reverse flow are detected in the TPIV velocity fields to present the breakdown positions, which further validates the result of dye streaklines. Comparisons and discussions are made on the results of flow visualization and TPIV measurement.

Dye visualization plays an important role on observing the LEV since its advantage of simplicity. Earlier investigators (Gursul and Yang 1995; Ol et al. 2003; Taylor et al. 2003) employed the dye visualization to investigate the oscillation of the breakdown position over a delta wing. In the current work, a 3D visualization method is developed, which provides a new way to quantitative investigate vortex breakdown positions. The breakdown positions could be recognized by investigating SIIs of the instantaneous streakline at different streamwise positions. The SII for a specific streamwise position is calculated by integrating the dye intensities in the corresponding $y-z$ planes. Variation of SII along x direction at different instantaneous times is provided in Fig. 6, which has a horizontal axis of time (t) and vertical axis of x location. The contours present the SII values, which are normalized by the largest value in the $t-x$ coordinates. It shows a dramatic increase in SII at a certain x location in an instantaneous time step. The increase in SII is believed indicating the vortex breakdown. The position of breakdown is therefore recognized by tracking the SII values downstream along streamwise direction and finding the first peak which is larger than a threshold of 0.2. The all-in-one method (Garcia 2011) is employed to smooth the contours and get the curve of time-sequent breakdown position as shown in Fig. 6 (black line). The line shows a periodical oscillation between $x = 87$ and $x = 118$ mm, sweeping a streamwise range of about 15.5 % c.

The corresponding frequency is estimated as 0.15–0.20 Hz, which corresponds to a Strouhal number ($S_t = fc/U_\infty$) of 0.50–0.67. The result is consistent with the low dominant frequency ($S_t = 0.63$) found at the LEV core for a similar non-slender delta wing by Gordnier and Visbal (2005).

Using dye streaklines to identify the breakdown types is a traditional approach (Lambourne and Bryer 1962; Lowson 1964; Payne et al. 1988). In the current work, the flow structures are clarified into three types: the spiral type, the transient type and the bubble type. The typical spiral type and bubble type with distinct characters are displayed in Fig. 4a and c. Besides these two types, there are also some instantaneous fields, which have no obvious features of spiral and bubble breakdowns. It is more like a transient status between two vortex breakdowns, which is named as transient type of breakdown in the current work. In Fig. 6, the breakdown types for different instantaneous times are marked on the breakdown position by hollowed circle (spiral type), cross (transient status) and solid square (bubble type). It shows that the spiral type happens more often than the bubble type, occupying 68 % of the whole measurement time interval. The bubble type usually happens when the breakdown point moves upstream and persists for short time before transforming into the spiral type, which has also been observed in the flows of slender delta wings (Gursul 2005).

Although the flow visualization method is simple and straightforward, it has some disadvantages. The dye streaklines present the traces of the flow particles, which have passed the upstream vortex core. When the breakdown positions or types have already been changed, the streaklines downstream the breakdown position might not change in time, which would lead to some misleading indications or deviations in breakdown positions. Therefore, besides giving the results from streaklines, further validation based on the TPIV velocity fields is necessary.

The vortex breakdown is usually characterized by the significant decrease in axial velocity (Gursul 2005). Fluctuation of axial velocity along the averaged LEV axis would provide important references for the vortex breakdown. In the current work, the LEV axis is extracted from the time-averaged Q fields by first finding the Q -peak positions at different y - z sections before vortex breakdown ($x < 87$) and then fitting the positions with a straight line. Figure 7 displays the time evolution of U_{axial} sampled from the LEV axis. The figure presents U_{axial} by contours, with a horizontal axis of time and a vertical axis of LEV core position. As expected, it shows that U_{axial} suffers a dramatic magnitude drop when tracking their values downstream along the LEV axis. The reverse flow, which corresponds to $U_{axial} \leq 0$, is normally believed as an important characteristic for breakdown and has been employed as a breakdown criterion following Oberleithner et al. (2012). A detection for reverse

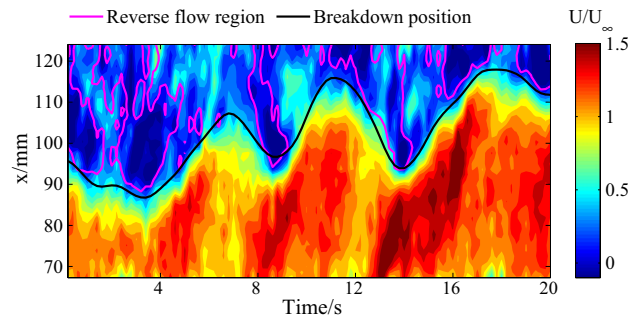


Fig. 7 U_{axial} contour and the reverse flow regions. The *contour* denotes the axial velocity, normalized by the free-stream velocity. The *magenta lines* show the streamwise ranges for reversed flow. The streakline-based breakdown positions are displayed by a *black line*

flow is made to find the streamwise range of reverse flow. Considering that the instantaneous LEV axis might deviate from its average place, the detection is performed in the neighboring zone of the averaged axis within a radius of 5 mm. The streamwise ranges for reverse flow are marked in the contour plot by magenta lines. For contrast, the streakline-based breakdown position line is also displayed in the plot by a black line. It shows that the oscillation trend of the breakdown line matches well with the positions where U_{axial} shows a steep drop along the streamwise direction. Furthermore, the reverse flow mostly occurs at locations close to the breakdown position line. Although streaklines and velocity fields represent the flow from different perspectives, they reach a good agreement in determining the breakdown positions.

3.4 Proper orthogonal decomposition on LEV based on Q criterion

Proper orthogonal decomposition (POD) is a common method to extract low-dimensional modes from high-dimensional systems (Chatterjee 2000). The method has been widely used to identify coherent structures in different turbulent flow phenomena (Berkooz et al. 1993; Venturi 2006; Feng et al. 2011). POD modes are highly associated with different energetic flow structures and sorted in order of their energies. By projecting the original velocity fields onto these POD modes, a series of POD coefficients is obtained, which describes the time-sequential energy fluctuation of the corresponding modes.

Kostas et al. (2005) compared the results of velocity-based and vorticity-based POD and concluded that the latter was more efficient in describing the dominant vortex structures. In the present work, it is believed that the Q fields are highly associated with LEV. Therefore, POD is directly performed based on 100 time-sequential volumetric Q fields, in order to extract some dominant modes of

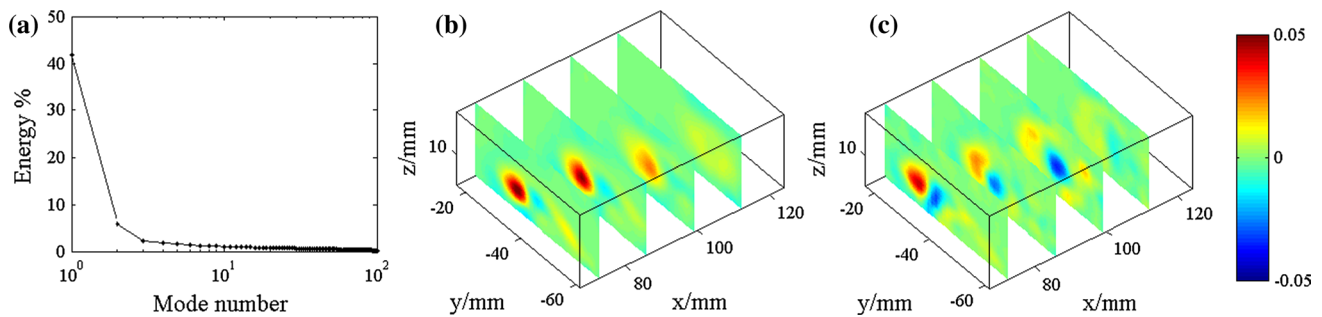


Fig. 8 POD energy percentages (a) and 1-th, 2-th POD mode (b, c)

LEV. All the POD modes and corresponding POD coefficients are normalized by their 2-norm. The energy percentages for POD modes are plotted in Fig. 8a. It shows a rapid energy decrease with increasing mode numbers, which is expectable in POD analysis. The energy percentages for the first two modes are significantly larger than other modes, reaching almost half of the total energy. Figure 8b and c visualizes the first two modes with contours of Q criterion at four spanwise and wall-normal sections along the streamwise direction at $x/c = 36.3, 42.9, 49.5, 56.1\%$, respectively. The first mode, which usually corresponds to the averaged field, appears as a clear vortex structure associated the LEV. The LEV in the first mode experiences a obvious strength decrease when it develops downstream, which is consistent with the observations on streamwise vorticity in Fig. 3. The second mode shows a pair of vortex tubes at the position of LEV along streamwise direction. It might be related to the wandering motion of LEV, which is an important phenomenon for the LEV (Gursul et al. 2005).

Regarding the vortex breakdown phenomenon, the 6-th and 7-th modes, a pair of conjugated POD modes, are observed. The two modes contribute similar energy percentages. Their vortex structures and POD coefficients are shown in Figs. 8a and 9, respectively. In Fig. 9a, the iso-surfaces of 6-th mode and 7-th mode are under the threshold of 0.01. Both modes show clear helical structures at the downstream of the vortex breakdown. The helical flow pattern is twisting and winding, which suggests that these two modes are highly related to the helical mode instability. Similar helical modes extracted by POD have also been reported by Wang and Gursul (2012), Roy and Leweke (2008), Del Pino et al. (2011). The corresponding POD coefficients shown in Fig. 9b indicate that the two modes have a temporal phase shift of about 90° . Due to our limited sampling frequency, the data do not have very fine temporal resolution. However, it is possible to estimate the dominant frequency of spiral breakdown as it will be further discussed in the late part of this subsection. The fluctuation of the POD coefficients seems intermittently coherent. For example, the curve at the interval of 0–5 s presents

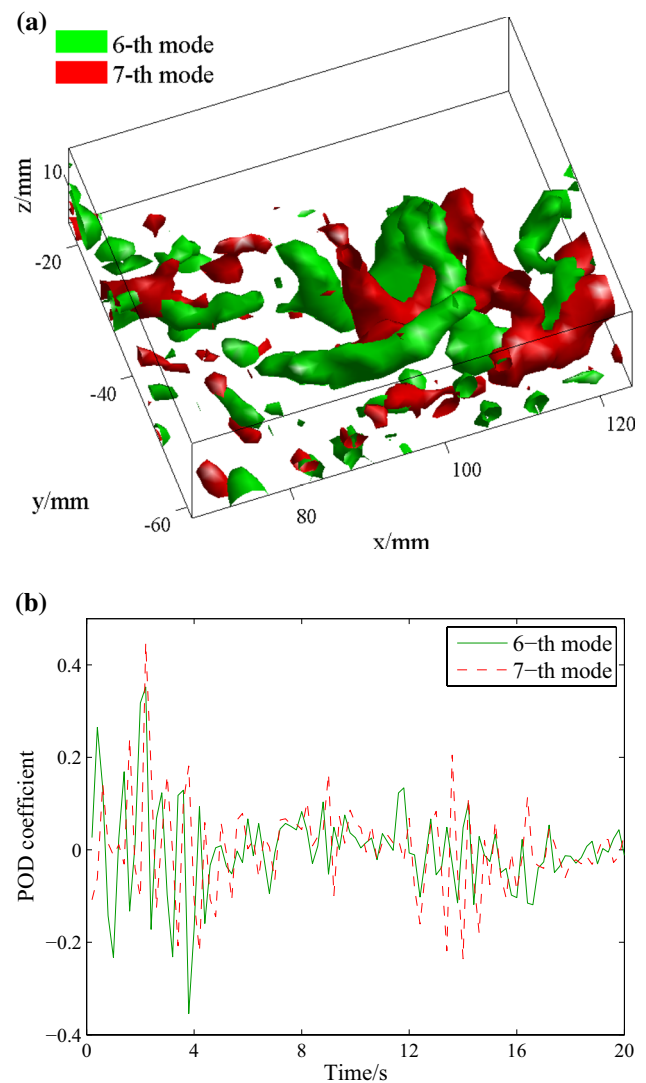


Fig. 9 The 6-th and 7-th POD modes (a) and corresponding POD coefficients (b)

a periodic variation, suggesting that a dominant frequency would occur there. The frequency is related to the helical mode instability (spiral breakdown) and is also equivalent

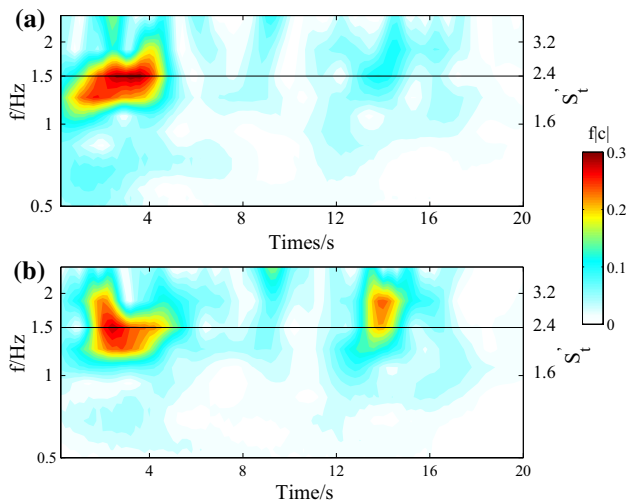


Fig. 10 Premultiplied wavelet spectra for 6-th (a) and 7-th (b) POD coefficients

to the angular frequency of helical swirl as described in Fig. 5.

Traditional Fourier transform is very popular for spectrum analysis. Unfortunately, it fails to extract the instantaneous frequency spectrum from a time-sequential signal. For this reason, it is not suitable for the current study, since spiral breakdown is intermittently happening at certain time segments, not lasting for the entire sampling period. Differently, wavelet transform provides an effective tool to extract a time-developing wavelet spectra, which contains all the frequency-energy information for a fixed time point. The advantage of wavelet transform benefits from the good time–frequency localization characteristic of wavelet bases, which is discussed in theory by Daubechies (1990). The wavelet transform for flow analysis has been widely applied (Farge 1992; Miao et al. 2004; Rinoshika and Zhou 2005).

Herein, the continuous wavelet transform (CWT) (Miao et al. 2004) is employed on the POD coefficients to obtain the corresponding wavelet spectra. The wavelet analysis is implemented using the wavelet tool in the MATLAB. The wavelet base is chosen as *cmor1-1.5* type in the family of complex Morlet wavelet, which is a common option for complex wavelet (Miao et al. 2004). Modulus of the wavelet coefficients ($|c|$) is correlated with the energy occupation for a specific frequency (f) at a certain time point. Results for CWT on the POD coefficients of 6-th mode and 7-th mode are displayed in Fig. 10. The figure adopts a logarithmic coordinate for the frequency axis to give more details of the low-frequency components. Premultiplied wavelet spectra are employed to ensure that equal areas of contours in Fig. 10 represent equal contributions to the total energy of the POD coefficients. It shows that the spectra for

6-th mode and 7-th mode are similar, both exhibiting high distribution at 0–5 s. The high distribution in the contour indicates a dominant frequency, which reveals the helical mode instability. Figure 6 also indicates that the high distributions in Fig. 10 mostly correspond to the occurrence of spiral breakdown. The averaged frequency of the high distribution areas ($f|c| > 0.2$) for 0–5 s is about 1.5 Hz, which is considered as the dominant frequency of the LEV spiral breakdown. The corresponding Strouhal number based on streamwise position and free-stream velocity ($S'_t = fx/U_\infty$) is about 2.4, which is similar to the result of (Gordnier and Visbal 2005) who obtained the Strouhal number of 2.8 by analyzing the frequency spectra of pressure coefficient at $x = 0.99 c$. The characteristic length scale in the current work is the center location of the measurement, which is $x = 0.48 c$. Gursul (1994) pointed out that $S'_t = fx/U_\infty$ is nearly constant for a given geometry of a slender delta wing at different streamwise locations, while the current study, however, was focused on a non-slender wing.

It is worth noting that the POD coefficients in Fig. 9b correspond to a helical mode with a fixed breakdown position as shown in Fig. 9a. During the measurement, the location of LEV breakdown was oscillating along the streamwise direction as shown in Fig. 6. When spiral vortex breakdown occurs and its breakdown position moves very far downstream, the correlation between the flow field and the conjugated POD modes would decrease, causing weak coherent variation in POD coefficients. Therefore, the wavelet method based on POD coefficients could not recognize all the time intervals for helical instability due to the offset of breakdown location to the POD modes, which could also be validated by comparing Fig. 10 with Fig. 6.

4 Conclusion

The current study achieved a simultaneous measurement of vortex breakdown over a non-slender delta wing with 3D flow visualization and TPIV. Techniques were developed to extract the dye images from the raw experimental images and reconstruct 3D dye streaklines using a traditional MART algorithm. The 3D dye streaklines clearly displayed the spatial shape of the LEV. The Q criterion was employed to identify the LEV from the TPIV velocity fields.

The time-averaged flow field was visualized by several spanwise and plane-normal sections of velocity and streamwise vorticity. A switching phenomenon of a jet-like profile to wake-like profile of axial velocity was observed. The combining of the two measurement methods shed light on a lot of details of the complex structures. Both spiral type and bubble type of breakdown were found by the two methods. The spiral type was characterized by a helical swirl with a sense opposite to the direction of the LEV swirl, inducing

low recirculating zones in the centerline. The bubble type was characterized by a suddenly expanding core, following by a tail at the rear. By extracting the skeletons of the 3D dye streaks, helical lines were obtained to represent the spatial motion of the helical swirl. The helical swirl rotated along the same direction with the LEV swirl. An inclined ellipse pattern was found in the axial view of helical lines.

The vortex breakdown positions were recognized by investigating the SII of streakline along streamwise direction. Oscillation of the breakdown positions was clearly observed, which had a low frequency of 0.15–0.20 Hz ($S_t = 0.50$ – 0.67) and was in a large streamwise range of about 15.5 % chord length. The breakdown types were identified according to the characteristics of streaklines. The breakdown positions were further validated by the U_{axial} contour plot and the reverse flow regions on it. The dye visualization based on SII and reverse flows in quantitative velocity fields shows a good agreement on locating the breakdown positions.

POD was directly performed on the Q fields calculated from TPIV results. The first two modes were related to the average LEV and its wandering motion along spanwise direction. A conjugated POD modes were obtained to describe the helical mode instability. The POD coefficients of the modes exhibited intermittently coherent fluctuations. Wavelet transform was employed to extract the dominant angular frequency of helical swirl, which was about 1.5 Hz ($S_t' = 2.4$). The high distribution areas on wavelet spectrum indicate the occurrence of spiral breakdown.

Acknowledgments This work was supported by the National Natural Science Foundation of China (11472030, 11327202, 11490552) and the Fundamental Research Funds for the Central Universities (YWF-16-JCTD-A-05).

References

- Berkooz G, Holmes P, Lumley JL (1993) The proper orthogonal decomposition in the analysis of turbulent flows. *Ann Rev Fluid Mech* 25(1):539–575
- Calderon DE, Wang Z, Gursul I (2012) Three-dimensional measurements of vortex breakdown. *Exp Fluids* 53(1):293–299
- Chatterjee A (2000) An introduction to the proper orthogonal decomposition. *Curr Sci* 78(7):808–817
- Chen H, Wang JJ (2014) Vortex structures for flow over a delta wing with sinusoidal leading edge. *Exp Fluids* 55(6):1761
- Daubechies I (1990) The wavelet transform, time-frequency localization and signal analysis. *Inf Theory IEEE Trans* 36(5):961–1005
- Del Pino C, Lopez-Alonso J, Parras L, Fernandez-Feria R (2011) Dynamics of the wing-tip vortex in the near field of a NACA 0012 aerofoil. *Aeronaut J* 115(1166):229
- Elsinga GE, Scarano F, Wieneke B, van Oudheusden BW (2006) Tomographic particle image velocimetry. *Exp Fluids* 41(6):933–947
- Escudier M (1988) Vortex breakdown: observations and explanations. *Prog Aerosp Sci* 25(2):189–229
- Farge M (1992) Wavelet transforms and their applications to turbulence. *Ann Rev Fluid Mech* 24(1):395–458
- Feng LH, Wang JJ, Pan C (2011) Proper orthogonal decomposition analysis of vortex dynamics of a circular cylinder under synthetic jet control. *Phys Fluids* (1994–present) 23(1):014,106
- Garcia D (2011) A fast all-in-one method for automated post-processing of PIV data. *Phys Fluids* 50(5):1247–1259
- Gordnier RE, Visbal MR (2005) Compact difference scheme applied to simulation of low-sweep delta wing flow. *AIAA J* 43(8):1744–1752
- Gursul I (1994) Unsteady flow phenomena over delta wings at high angle of attack. *AIAA J* 32(2):225–231
- Gursul I (2005) Review of unsteady vortex flows over slender delta wings. *J Aircraft* 42(2):299–319
- Gursul I, Gordnier R, Visbal M (2005) Unsteady aerodynamics of non-slender delta wings. *Prog Aero Sci* 41(7):515–557
- Gursul I, Taylor G, Wooding C (2002) Vortex flows over fixed-wing micro air vehicles. In: *AIAA Paper* 698, p 2002
- Gursul I, Yang H (1995) On fluctuations of vortex breakdown location. *Phys Fluids* (1994–present) 7(1):229–231
- Hall M (1972) Vortex breakdown. *Ann Rev Fluid Mech* 4(1):195–218
- Hunt J, Wray A, Moin P (1988) Eddies, stream, and convergence zones in turbulent flows. In: *Center for turbulence research report*. Center for Turbulence Research, Stanford, USA, CTR-S88, pp 193–208
- Jumper E, Nelson R, Cheung K (1993) A simple criterion for vortex breakdown. In: *AIAA paper*, pp 93–0866
- Kerschnitzki M, Kollmannsberger P, Burghammer M, Duda GN, Weinkamer R, Wagermaier W, Fratzl P (2013) Architecture of the osteocyte network correlates with bone material quality. *J Bone Miner Res* 28(8):1837–1845
- Kostas J, Soria J, Chong M (2005) A comparison between snapshot POD analysis of PIV velocity and vorticity data. *Exp Fluids* 38(2):146–160
- Lambourne N, Bryer D (1962) The bursting of leading-edge vortices: some observations and discussion of the phenomenon. *HM Stationery Office*
- Lee TC, Kashyap RL, Chu CN (1994) Building skeleton models via 3-D medial surface axis thinning algorithms. *CVGIP Graph Models Image Process* 56(6):462–478
- Lessen M, Singh PJ, Paillet F (1974) The stability of a trailing line vortex. Part 1. Inviscid theory. *J Fluid Mech* 63(04):753–763
- Lowson M (1964) Some experiments with vortex breakdown (water tunnel flow visualization on slender delta wings reveal vortex breakdown formation to be a nonaxisymmetric stability). *R Aeronaut Soc J* 68:343–346
- Lucca-Negro O, O’Doherty T (2001) Vortex breakdown: a review. *Prog Energy Combust Sci* 27(4):431–481
- Miau JJ, Wu SJ, Hu CC, Chou JH (2004) Low-frequency modulations associated with vortex shedding from flow over bluff body. *AIAA J* 42(7):1388–1397
- Oberleithner K, Paschereit C, Seele R, Wygnanski I (2012) Formation of turbulent vortex breakdown: intermittency, criticality, and global instability. *AIAA J* 50(7):1437–1452
- Ol MV, Gharib M, Ol MV, Gharib M (2003) Leading-edge vortex structure of non-slender delta wings at low Reynolds number. *AIAA J* 41(1):16–26
- Payne F, Ng T, Nelson R, Schiff L (1988) Visualization and wake surveys of vortical flow over a delta wing. *AIAA J* 26(2):137–143
- Pereira F, Gharib M (2002) Defocusing digital particle image velocimetry and the three-dimensional characterization of two-phase flows. *Meas Sci Technol* 13(5):683
- Rinoshika A, Zhou Y (2005) Orthogonal wavelet multi-resolution analysis of a turbulent cylinder wake. *J Fluid Mech* 524:229–248
- Roy C, Leweke T (2008) Experiments on vortex meandering. In: *FAR-Wake Technical Report* AST4-CT-2005-012238,

- CNRS-IRPHE, also presented in international workshop on fundamental issues related to aircraft trailing wakes, pp 27–29
- Scarano F (2002) Iterative image deformation methods in PIV. *Meas Sci Technol* 13(1):R1
- Scarano F (2013) Tomographic PIV: principles and practice. *Meas Sci Technol* 24(1):12001–12028
- Srinivas S, Gursul I, Batta G (1994) Active control of vortex breakdown over delta wings. In: AIAA Paper, pp 94–2215
- Taylor GS, Gursul I (2004) Buffeting flows over a low-sweep delta wing. *AIAA J* 42(9):1737–1745
- Taylor G, Schnorbus T, Gursul I (2003) An investigation of vortex flows over low sweep delta wings. In: AIAA Paper 4021, p 2003
- Towfighi J, Rockwell D (1993) Instantaneous structure of vortex breakdown on a delta wing via particle image velocimetry. *AIAA J* 31(6):1160–1162
- Venturi D (2006) On proper orthogonal decomposition of randomly perturbed fields with applications to flow past a cylinder and natural convection over a horizontal plate. *J Fluid Mech* 559:215–254
- Wang C, Gao Q, Wang H, Wei R, Li T, Wang J (2016) Divergence-free smoothing for volumetric PIV data. *Exp Fluids* 57(1):1–23
- Wang Z, Gursul I (2012) Unsteady characteristics of inlet vortices. *Exp Fluids* 53(4):1015–1032
- Wang JJ, Zhang W (2008) experimental investigations on leading-edge vortex structures for flow over non-slender delta wings. *Chin Phys Lett* 25(7):2550–2553
- Wieneke B (2008) Volume self-calibration for 3D particle image velocimetry. *Exp Fluids* 45(4):549–556
- Yaniktepe B, Rockwell D (2004) Flow structure on a delta wing of low sweep angle. *AIAA J* 42(3):513–523